

# Final Report

## Magnetism and superconductivity in intermetallic nanocomposites

Consortial OTKA project K115575 and K115632

Principal investigators: László Szunyogh and Balázs Újfalussy

In this Final Report we sort our work we carried out during the five years of the project following the main topics outlined in the research plan. The numbers in the square brackets correspond to those in the list of publications attached to this report.

### 1. Heusler alloys and exchange bias effect

Within the program of our European research project HRFIR finished by Mar 31, 2017 we performed a systematic study of the magnetic ground state and finite temperature magnetism of ordered and disordered  $\text{Ni}_2\text{MnAl}$  full Heusler compounds. By increasing the degree of the long-range chemical disorder between the Mn and Al sublattices, the magnetic order progressively changed from the ferromagnetic state in the ordered  $L2_1$  phase toward a fully compensated antiferromagnetic state in the disordered B2 phase. In the disordered compounds, strong antiferromagnetic site-antisite Mn-Mn interactions appeared. In view of potential applications of disordered  $\text{Ni}_2\text{MnAl}$  as a room temperature antiferromagnet, we calculated the magnetic anisotropy energies of tetragonally distorted samples in the B2 phase and found that they are smaller by two orders in magnitude than in the frustrated antiferromagnet  $\text{IrMn}_3$ . [1] Combining *ab initio* methods with spin dynamics simulations, we investigated the magnetic behavior of  $\text{Ni}_2\text{MnAl}/\text{Fe}$  bilayers. Our simulations show that such a bilayer exhibits a small exchange bias effect when the  $\text{Ni}_2\text{MnAl}$  Heusler alloy is in a disordered B2 phase. Additionally, we presented an effective way to control the magnetic structure of the  $\text{Ni}_2\text{MnAl}$  antiferromagnet, in the pseudo-ordered B2-I as well as the disordered B2 phases, via a spin-flop coupling to the Fe layer. [21]

We showed that the transition from antiferromagnetic order in  $\text{Ru}_2\text{MnGe}$  to ferromagnetic order in vanadium substituted  $\text{Ru}_2\text{Mn}_{1-x}\text{V}_x\text{Ge}$  is due to a progressive increase of the first-nearest neighbor (NN) ferromagnetic coupling between Mn atoms. Using *ab-initio* calculated exchange parameters and performing finite temperature Monte Carlo simulations on a disordered lattice, we described the experimental magnetic phase diagram for the full range of vanadium concentrations, including the variation of the ordering temperature and the onset of finite magnetization in the ground state. Since the observed changes in the Mn-Mn magnetic interactions are continuous with increasing V content, we argued that there is a threshold concentration of V substitutions where the critical fluctuations associated with frustration effects on the fcc lattice could be studied experimentally. [23]

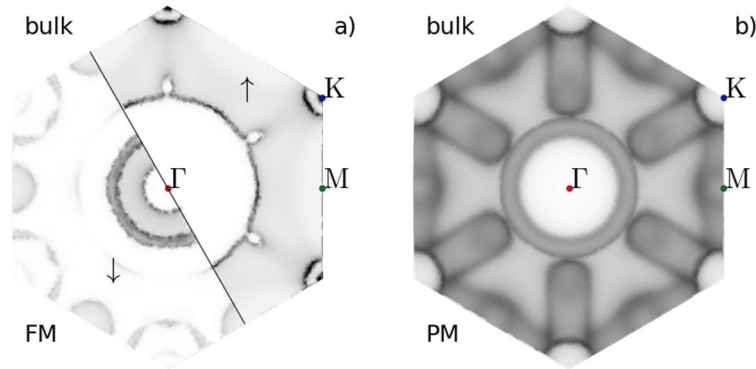
Motivated by previous experiments displaying a huge exchange bias effect in polycrystalline MnN/Fe samples, we performed a detailed study on the magnetic properties of bulk MnN and of the MnN/Fe interface. For the  $\theta$ -phase of bulk MnN we found that the competition between the nearest and the next-nearest-neighbor interactions leads to antiferromagnetic ordering of the Mn spins, in agreement with previous theoretical and experimental results. At the MnN/Fe interface, a sizable Dzyaloshinsky-Moriya (DM) interaction appears leading to a stable exchange-bias effect. We studied the dependences of the exchange-bias effect on the thicknesses of the ferromagnetic and the antiferromagnetic layers and compared them to experimentally obtained results. [27]

We summarized our results achieved with the HRFIR project in the review article [17].

## 2. Finite temperature magnetism

### a. Bulk magnetism

By calculating the spectral density of states in the ferromagnetic ground state and in the high temperature paramagnetic phase we provided the first concise study of finite temperature effects on the electronic structure of the bulk and the surface of Gadolinium metal. The variation of calculated spectral properties of the Fermi surface and the density of states in the bulk and at the surface are in good agreement with recent photoemission experiments performed in both ferromagnetic and paramagnetic phases. We clearly demonstrated that the formation of local spin moments in the conduction band is due to the asymmetry of the density of states in the two spin channels, suggesting a complex non-Stoner behavior. [2]



(a) Spin resolved spectral DOS of the ferromagnetic phase and (b) total spectral DOS of the paramagnetic phase of bulk Gadolinium at the Fermi energy as projected to the 2D Brillouin zone. Darker colors represent larger values of the spectral DOS. [2]

We demonstrated that uniaxial tensile strain can destabilize the magnetic order in bulk iron and decrease the Curie temperature. In consequence, the intrinsic strength of the ideal single-crystal body-centered cubic iron dramatically weakens above a critical temperature of  $\sim 500$  K. The discovered strain-induced magneto-mechanical softening provides a plausible atomic-level mechanism behind the observed drop of the measured strength of Fe whiskers around 300–500 K. Alloying, which has the capability to partially restore the magnetic order in the strained Fe lattice, push the critical temperature for the strength-softening scenario towards the magnetic transition temperature of the undeformed lattice. This can result in a surprisingly large alloying-driven strengthening effect at high temperature as illustrated in the case of Fe-Co alloy. [4]

We investigated the thermal magnetic properties of the ferrimagnetic rare-earth transition-metal intermetallic  $\text{DyCo}_5$  and compared our theoretical findings to elemental resolved measurements on  $\text{DyCo}_5$  thin films using the x-ray magnetic circular dichroism technique. With our model, we were able to accurately compute the complex temperature dependence of the magnetization. We found a spin reorientation transition (SRT) as a consequence of competing elemental magneto-crystalline anisotropies in connection with different degrees of thermal demagnetization in the Dy and Co sublattices. [15]

### b. Spin reorientations and magnetic switching

Fe/MgO-based magnetic tunnel junctions are among the most promising candidates for spintronic devices due to their high thermal stability and high tunneling magnetoresistance. We investigated the electronic, structural, and magnetic properties of MgO/Fe/MgO sandwiches using first-principles calculations and atomistic spin modeling based on a fully parametrized spin Hamiltonian. We found a large contribution to the effective interfacial magnetic anisotropy from the two-ion exchange energy.

Minimization of the total energy using atomistic simulations showed a surprising spin-spiral ground-state structure at the interface owing to frustrated ferromagnetic and antiferromagnetic interactions, leading to a reduced Curie temperature and strong layerwise temperature dependence of the magnetization. The different temperature dependences of the interface and bulk-like layers result in an unexpected nonmonotonic temperature variation of the effective magnetic-anisotropy energy and temperature-induced spin-reorientation transition to an in-plane magnetization at low temperatures. [26]

We studied the complex magnetic properties of Fe/Ir/Fe sandwiches using a hierarchical multi-scale model. Based on first principles calculations and thermodynamic models we revealed the equilibrium spin-wave, magnetization and dynamic demagnetization properties. Finite temperature calculations showed a complex spin-wave dispersion and an initially counter-intuitive, increasing exchange stiffness with temperature (a key quantity for device applications) due to the effects of frustration at the interface, which then decreases due to magnon softening. Finally, the demagnetization process in these structures is shown to be much slower at the interface as compared with the bulk, a key insight to interpret ultrafast laser-induced demagnetization processes in layered or interface materials. [25] Based on numerical simulations, we demonstrated thermally induced magnetic switching in synthetic ferrimagnets composed of multilayers of rare-earth and transition metals. Our findings show that deterministic magnetization reversal occurs above a certain threshold temperature if the ratio of transition-metal atoms to rare-earth atoms is sufficiently large. Surprisingly, the total thickness of the multilayer system has little effect on the occurrence of switching. We also provided a simple argument to explain the temperature dependence of the reversal process. [16]

### c. Method developments

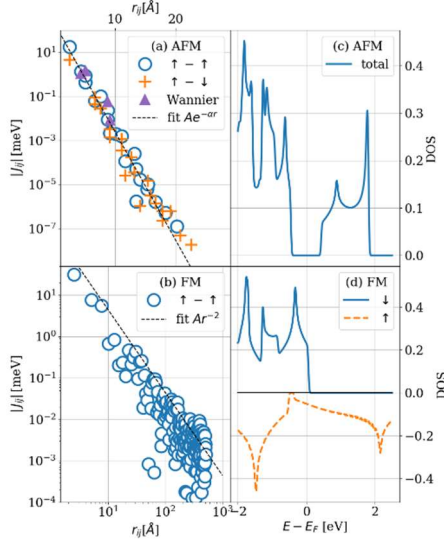
In the multiscale modelling of magnetic materials, it is essential to take into account the temperature dependence of the interaction parameters entering the micromagnetic models. We investigated the temperature dependence of the effective Dzyaloshinsky-Moriya interaction by calculating the spin wave dispersion relation of ferromagnets from finite-temperature spin dynamics simulations. We have shown that the DM interaction behaves similarly to the Heisenberg exchange interaction, while the effective on-site anisotropy constant decreases faster with temperature. We calculated corrections in the temperature dependence of the interaction parameters with respect to the random phase approximation due to spin-spin correlations based on Green's function theory, showing good quantitative agreement with the simulation results. We found that the DM interaction leads to the appearance of an additional anisotropy term which increases with temperature at high magnetization values, in contrast to the conventional on-site anisotropy term. [19]

In the spirit of multi-scale modelling magnetization dynamics at elevated temperature is often simulated in terms of a spin model where the model parameters are derived from first principles. While these parameters are mostly assumed temperature-independent and thermal properties arise from spin fluctuations only, other scenarios are also possible. Choosing bcc Fe as an example, we investigated the influence of different kinds of model assumptions on ultrafast spin dynamics, where following a femtosecond laser pulse, a sample is demagnetized due to a sudden rise of the electron temperature. While different model assumptions do not affect the simulation results qualitatively, their details do depend on the nature of the modelling. [14]

We employed metadynamics simulations to calculate the free-energy landscape of thin ferromagnetic films and performed a systematic study of the temperature dependence of magnetic anisotropy and of the spin-reorientation transitions. By using a simple spin model we recovered the well-known power-law behavior of the magnetic anisotropy energy against magnetization and presented a rather detailed analysis of the SRT in ultrathin films. Based on tensorial exchange interactions and anisotropy parameters derived from first-principles calculations, we performed simulations for Fe double layers deposited on Au(001) and W(110). In the case of a double Fe layer on W(110), our simulations displayed an out-of-plane to in-plane spin-reorientation transition in agreement with experiments. [44]

Based on a nonorthogonal basis set we presented a computational method to determine the exchange constants in isotropic spin models and implemented it in the SIESTA code. We used the new method

to study the sp magnetism in graphene nanostructures. For fluorinated graphene we obtained exchange interactions in fairly good agreement with previous calculations using maximally localized Wannier functions, see the figure below, and we confirmed the theoretical prediction of a  $120^\circ$  Néel state. Associated with the magnetic edge states of a zigzag graphene nanoribbon we found rapidly decaying exchange interactions with an unconventional distance dependence. We showed that the stiffness constant derived from the exchange interactions is consistent with a previous estimate based on total energy differences of twisted spin configurations. [47]



(a) and (b) Magnitudes of the exchange interactions between magnetic carbon atoms as a function of the distance in fluorinated graphene in the row-wise AFM and in the FM states, respectively. Blue circles denote interactions between atoms with the same magnetic orientation, orange crosses denote interactions between moments with opposite orientation, while purple triangles stand for the interactions reported in the work of A. N. Rudenko et al., Phys. Rev. B **88**, 081405(R) (2013). Note that (a) is plotted on a log-linear scale, while (b) on a log-log scale. The total density of states for the AFM state and the spin-resolved densities of states for the FM state in the vicinity of the Fermi level are plotted in (c) and (d), respectively. [47]

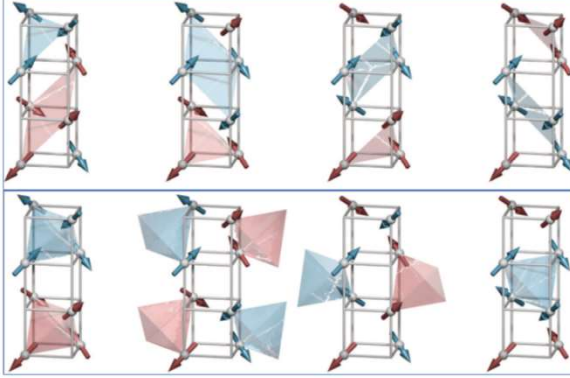
### 3. Noncollinear magnetism

#### a. Bulk systems with complex magnetic ground state

We presented combined spin model and first-principles electronic-structure calculations to study the *weak ferromagnetism* in bulk  $Mn_3Z$  ( $Z = Sn, Ge, Ga$ ) compounds. The spin-model parameters were determined from a spin-cluster expansion technique based on the relativistic disordered local moment formalism. We described the magnetic ground state of the system within a three-sublattice model and investigated the formation of the weak ferromagnetic states in terms of the relevant model parameters. First, we gave a group-theoretical argument how the point-group symmetry of the lattice leads to the formation of weak ferromagnetic states. Then we studied the ground states of the classical spin model and derived analytical expressions for the weak ferromagnetic distortions by recovering the main results of the group-theoretical analysis. As a third approach, we obtained the weak ferromagnetic ground states from selfconsistent density-functional calculations and compared our results with previous first-principles calculations and with available experimental data. We demonstrated that the orbital moments follow a decomposition predicted by group theory. For a deeper understanding of the formation of weak ferromagnetism, we selectively traced the effect of the spin-orbit coupling at the Mn and Z sites. In case of  $Mn_3Ga$ , we also studied the role of the induced moment of Ga from constrained local density-functional calculations. [45]

Still related to the HARFIR project mentioned in Section 1 we investigated the magnetic properties of  $Ru_2MnZ$  ( $Z = Sn, Sb, Ge, Si$ ) chemically ordered, full Heusler compounds for zero as well as finite temperatures. Based on first-principles calculations we derived the interatomic isotropic bilinear and biquadratic couplings between Mn atoms from the paramagnetic state. We found frustrated isotropic couplings for all compounds and, in the case of  $Z = Si$  and  $Sb$ , a nearest-neighbor biquadratic coupling that favored perpendicular alignment between the Mn spins. By using an extended classical Heisenberg model in combination with spin dynamics simulations we obtained the magnetic equilibrium states. From these simulations we concluded that the biquadratic coupling, in combination with the frustrated isotropic interactions, leads to noncollinear magnetic ground states in the  $Ru_2MnSi$

and Ru<sub>2</sub>MnSb compounds. In particular, for these alloys we found two distinct, noncollinear ground states which are energetically equivalent and can be identified as 3Q and 4Q states on a frustrated fcc lattice, see the figure below. Investigating the thermal stability of the noncollinear phase we found that, in the case of Ru<sub>2</sub>MnSi, the multiple-Q phase undergoes a transition to the single Q phase, while in case of Ru<sub>2</sub>MnSb the corresponding transition is not obtained due to the larger magnitude of the nearest-neighbor biquadratic coupling. [54]



Magnetic ground state configurations simulated for Ru<sub>2</sub>MnZ (Z =Si,Sb) Heusler compounds with negative NN biquadratic coupling. The upper panel shows different variations of 3Q states, where the fully compensated (111) planes are indicated with red and blue colors. In the lower panel different variations of 4Q states can be seen, with fully compensated tetrahedra indicated by red and blue colors. [54]

## b. Domain walls and spin-spiral states in thin films

We performed a study of domain walls in Co/Ir<sub>n</sub>/Pt(111) ( $n = 0, \dots, 6$ ) films by a combined approach of first-principles calculations and spin-dynamics simulations. We determined the tensorial exchange interactions and the magnetic anisotropies for the Co overlayer in both fcc and hcp geometries, depending on the number of Ir buffer layers. We found strong ferromagnetic nearest-neighbor isotropic exchange interactions between the Co atoms and an out-of-plane magnetic anisotropy for the films in fcc geometry. Our simulations show that the magnetic domain walls are of Néel type, and their rotational sense (chirality) is changed upon the insertion of an Ir buffer layer compared to the pristine Co/Pt(111) system. Our spin-dynamics simulations indicate a twisting of the spins with respect to the planar domain-wall profile on the triangular lattice. We discuss this domain-wall twisting using symmetry arguments and in terms of an appropriate micromagnetic continuum model considering extra energy terms compared to the available literature. [12]

Using first-principles calculations, we studied the magnetic interactions in a Co monolayer on a Pt(111) surface with a capping monolayer of selected 5*d* elements (Re, Os, Ir, Pt, and Au). We found a close relationship between the magnetic moment of the Co atoms and the nearest-neighbor isotropic exchange interaction, which is attributed to the electronic hybridization between the Co and the capping layers, in the spirit of the Stoner picture of ferromagnetism. The Dzyaloshinsky-Moriya interaction is decreased for all overlayers compared to the uncapped Co/Pt(111) system, while even the sign of the DM interaction changes in the case of the Ir overlayer. We concluded that the variation of the DM interaction was well correlated with the change of the magnetic anisotropy energy and of the orbital moment anisotropy. The unique influence of the Ir overlayer on the DM interaction is traced by scaling the strength of the spin-orbit coupling of the Ir atoms in Ir/Co/Pt(111) and by changing the Ir concentration in the Au<sub>1-x</sub>Ir<sub>x</sub>/Co/Pt(111) system. Our spin dynamics simulations indicate that the magnetic ground state of Re/Co/Pt(111) thin film is a spin spiral with a tilted normal vector, while the other systems are ferromagnetic. [40]

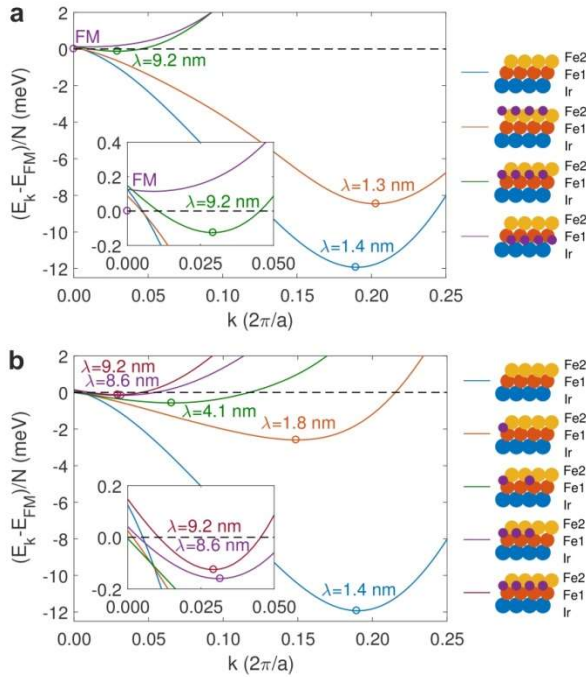
Based on the Korringa-Kohn-Rostoker Green's function technique, we presented a computational scheme for calculating the electronic structure of layered systems in a homogeneous spin-spiral magnetic state. From the self-consistent nonrelativistic calculations, the total energy of the spin-spiral states was determined as a function of the wave vector, while a relativistic extension of the formalism in first order of the spin-orbit coupling gave an access to the effect of the Dzyaloshinsky-Moriya interactions. We demonstrated that the newly developed method properly described the magnetic ground state of a Mn monolayer on W(001) and of a Co monolayer on Pt(111). The obtained spin-spiral energies were mapped to a classical spin model, the parameters of which were compared to

those calculated directly from the relativistic torque method. In case of a Co monolayer on Pt(111), we found that the isotropic interaction between the Co atoms was reduced and the DM interaction was increased when capped by a Ru layer. In addition, we performed spin-spiral calculations on the Ir/Fe/Co/Pt and Ir/Co/Fe/Pt multilayer systems and found a spin-spiral ground state with very long wavelength due to the frustrated isotropic couplings between the Fe atoms, whereas the DM interaction was strongly influenced by the sequence of the Fe and Co layers. [46]

Spin-polarized scanning tunneling microscopy investigations revealed a significant increase of the magnetic period of spin spirals in three-atomic-layer-thick Fe films on Ir(111), from about 4 nm at 8 K to about 65 nm at room temperature. We attributed this considerable influence of temperature on the magnetic length scale of noncollinear spin states to different exchange interaction coefficients in the different Fe layers. We thus proposed a classical spin model that reproduced the experimental observations and in which the crucial feature is the presence of magnetically coupled atomic layers with different interaction strengths. [13]

### c. Magnetic skyrmions: experiment and theory

Magnetic skyrmions are expected to be used as bits of information in future magnetic data storage devices. An essential step toward future skyrmion-based applications is to engineer key magnetic parameters for developing and stabilizing individual magnetic skyrmions. Our experimental coworkers at the University of Hamburg demonstrated the tuning of the non-collinear magnetic state of an Fe double layer on an Ir(111) substrate by loading the sample with atomic hydrogen. By using spin-polarized scanning tunneling microscopy, they discovered that the hydrogenated system supports the formation of skyrmions in external magnetic fields, while the pristine Fe double layer does not. Based on ab initio calculations, we attributed this effect to the tuning of the Heisenberg exchange and the Dzyaloshinsky–Moriya interactions due to hydrogenation. [31]



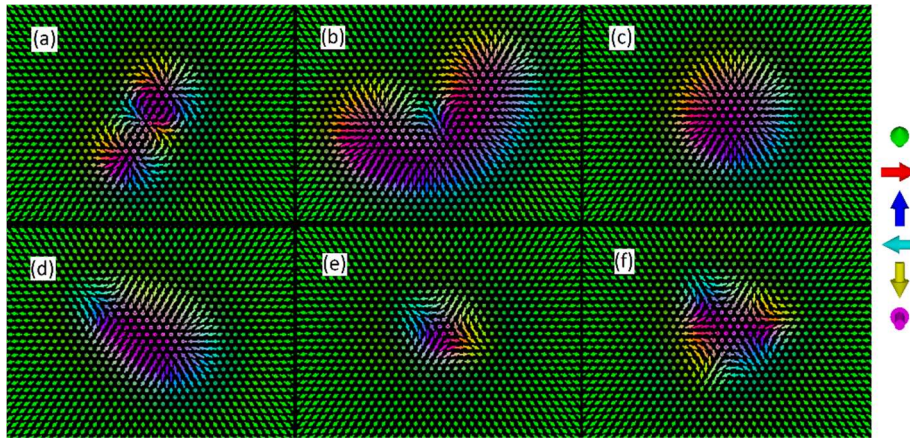
Influence of the H adsorption site and H concentration on the magnetic ground state from ab initio calculations. Energies of harmonic cycloidal spin spiral states per spin as a function of wave vector along the  $[11\bar{2}]$  direction compared to the ferromagnetic state. a, Dependence on adsorption site. From top to bottom in the legend: Fe double layer, H above the Fe layers in fcc hollow sites, H between the Fe layers in octahedral sites, and H between Ir and Fe in octahedral sites. b, Dependence on H concentration. The concentration increases in steps of 0.25 ML from top to bottom in the legend. Circles denote the location of the minima converted to the magnetic period length  $\lambda = 2\pi / k$ , with the lattice constant  $a = 2.71 \text{ \AA}$ . The energy of the spiral at zero wave vector differs from that of the ferromagnetic state due to the magnetic anisotropy energy. [31]

In searching the conditions of the formation of magnetic skyrmions we determined the magnetic B-T phase diagram of PdFe bilayer on Ir(111) surface by performing Monte Carlo and spin dynamics simulations based on an effective classical spin model. At low temperatures we found three types of ordered phases, namely, a spin-spiral phase, a skyrmion lattice phase and a fully polarized state, while at higher temperatures, below the completely disordered paramagnetic phase, a large region of the phase diagram is associated with a fluctuation-disordered phase. Within the applied model, this state is

characterized by the presence of skyrmions with finite lifetime. According to the simulations, this lifetime follows the Arrhenius law as a function of temperature. [10]

We determined the parameters of a classical spin Hamiltonian describing an Fe monolayer on Pd(111) surface with a  $\text{Pt}(1-x)\text{Ir}_x$  alloy overlayer from ab initio calculations. While the ground state of the system is ferromagnetic for  $x=0.00$ , it becomes a spin spiral state as Ir is intermixed into the overlayer. Although the Dzyaloshinsky-Moriya interaction is present in the system, we demonstrated that the frustrated isotropic exchange interactions play a prominent role in creating the spin spiral state, and these frustrated couplings lead to an attractive interaction between skyrmions at short distances. Using spin dynamics simulations, we showed that under these conditions the individual skyrmions form clusters, and that these clusters remain stable at finite temperature. [11]

We observed metastable localized spin configurations with topological charges ranging from  $Q = -3$  to  $Q = 2$  in a  $(\text{Pt}_{0.95}\text{Ir}_{0.05})/\text{Fe}$  bilayer on a Pd(111) surface, see figure below. We demonstrated that the frustration of the isotropic exchange interactions is responsible for the creation of these various types of skyrmionic structures. The Dzyaloshinsky-Moriya interaction present due to the breaking of inversion symmetry at the surface energetically favored skyrmions with  $Q = -1$ , distorted the shape of the other objects, and defined a preferred orientation for them with respect to the underlying lattice. [22]



Metastable localized spin-configurations with different topological charges: (a) skyrmion with  $Q = -3$ , (b) skyrmion with  $Q = -2$ , (c) skyrmion with  $Q = -1$ , (d) chimeral skyrmion with  $Q = 0$ , (e) antiskyrmion with  $Q = 1$ , and (f) antiskyrmion with  $Q = 2$ . The value of the external field is  $B = 2.35\text{T}$  in part (a) and  $B = 0.23\text{T}$  in parts (b)-(f); the ground state is field-polarized for  $B > 0.21\text{T}$ . The colors indicate the directions of the spin vectors, illustrated on the right edge of the figure. [22]

In addition to  $1\pi$  skyrmions investigated in most experimental and theoretical studies, the magnetization direction may rotate multiple times going from the center of the structure towards the ferromagnetic background, leading to the appearance of  $k\pi$  skyrmions. Using spin dynamics simulations, we investigated the stability of  $1\pi$ ,  $2\pi$  and  $3\pi$  skyrmions in the Pd/Fe/Ir(111) system where the presence of  $1\pi$  skyrmions was already demonstrated experimentally. We determined the magnetic field ranges where skyrmionic structures with various orders  $k$  may be stabilized in the system, along with the energy barriers protecting these structures. We also demonstrated a mechanism of switching between skyrmionic structures with different orders  $k$  in disk-shaped samples via an instantaneous reversal of the external magnetic field. [32] Moreover, we analyzed the localized magnon modes of isolated  $k\pi$  skyrmions on a field-polarized background based on the Landau-Lifshitz-Gilbert equation with an atomistic classical spin model. For increasing skyrmion order  $k$  we found a higher number of excitation modes, including modes with nodes in the radial eigenfunctions. We showed that at low fields  $2\pi$  and  $3\pi$  skyrmions are destroyed via a burst instability connected to a breathing mode, while  $1\pi$  skyrmions undergo an elliptic instability. At high fields all  $k\pi$  skyrmions collapse due to the instability of a breathing mode. We calculated the effective damping parameters of the spin waves in the low Gilbert damping limit and found them to diverge in the case of the lowest-

lying modes at the burst and collapse instabilities but not at the elliptic instability. We also showed that the breathing modes of  $k\pi$  skyrmions may become overdamped at higher Gilbert damping values. [34]

Damping mechanisms in magnetic systems determine the lifetime, diffusion, and transport properties of magnons, domain walls, magnetic vortices, and skyrmions. Based on the phenomenological Landau-Lifshitz-Gilbert equation, we determined the effective damping parameter in noncollinear magnetic systems describing the linewidth in resonance experiments or the decay parameter in time-resolved measurements. We explored how the effective damping can be calculated from the elliptic polarization of magnons, arising due to the noncollinear spin arrangement. We concluded that the effective damping is larger than the Gilbert damping, and it may significantly differ between excitation modes. We presented numerical results for the effective damping for the localized magnons in isolated skyrmions, with parameters based on the Pd/Fe/Ir(111) model-type system. [35]

In terms of micromagnetic simulations we showed that ensembles of magnetic skyrmions in confined geometries exhibit thermally driven motion on two different time scales. The intrinsic fluctuating dynamics ( $t \sim 1$  ps) are governed by short-range symmetric and antisymmetric exchange interactions, whereas the long-time limit ( $t \gtrsim 10$  ns) is determined by the coaction of skyrmion-skyrmion-repulsion and the system's geometry. We demonstrated how the competition between skyrmion mobility and observation time directly affects the addressability of skyrmionic bits, which is a key challenge on the path of developing skyrmion-based room-temperature applications. The presented quasiparticle Monte Carlo approach offers a computationally efficient description of the diffusive motion of skyrmion ensembles in confined geometries, like racetrack memory setups. [42]

#### **d. Theoretical STM investigation of magnetic skyrmions**

We introduced a method for a combined calculation of charge and vector spin transport of elastically tunneling electrons in magnetic scanning tunneling microscopy (STM). As an application, we analyzed the STM contrast inversion of the charge current above the Fe/W(110) surface depending on the bias voltage, tip-sample distance and relative magnetization orientation between the sample and an iron tip. For the spin transfer torque (STT) vector we found that its in-plane component is generally larger than the out-of-plane component. Our results suggest that the torque-current relationship in magnetic STM junctions follows the power law rather than a linear function. Consequently, we show that the ratio between the STT and the spin-polarized charge current can be tuned by the bias voltage, tip-sample distance and magnetization rotation. We demonstrated the possible enhancement of the STT efficiency in magnetic STM junctions, which can be exploited in technological applications. [9]

By performing spin-polarized scanning tunneling microscopy (SP-STM) calculations, we reported on the characterization of metastable skyrmionic spin structures with various topological charges ( $Q = -3, -2, -1, 0, +1, +2$ ) in the  $(\text{Pt}_{1-x}\text{Ir}_x)\text{Fe}/\text{Pd}(111)$  ultrathin magnetic film. We found that an out-of-plane magnetized tip already results in distinguished SP-STM contrasts for the different skyrmionic structures corresponding to their symmetries. For spin structures exhibiting a uniform sign of the local vorticity throughout the whole skyrmionic area, we demonstrated that (i)  $|Q|$  can be determined from a single SP-STM image taken by any in-plane magnetized tip and (ii) an in-plane tip magnetization rotation provides the sign of  $Q$  independently of the sign of the effective spin polarization in the tunnel junction. We also discussed cases where the local vorticity is changing sign. [18]

We studied the tunneling spin transport characteristics of a magnetic skyrmion in spin-polarized scanning tunneling microscopy. The theory development included the combined description of the charge current and tunneling spin transport vector quantities: the longitudinal spin current and the spin transfer torque, all in high spatial resolution. Connections between the conventional charge current SP-STM image contrasts and the magnitudes of the spin transport vectors were demonstrated that enables the estimation of tunneling spin transport properties based on experimentally measured SP-STM images. A considerable tunability of the spin transport vectors by the involved spin polarizations was also highlighted. [37]

Based on a combined charge and vector spin transport theory capable of imaging noncollinear magnetic textures on surfaces with spin-polarized scanning tunneling microscopy, we investigated the high-resolution tunneling electron charge and coupled spin transport properties of a variety of Néel- and Bloch-type skyrmions. Axially symmetric skyrmions are considered within the same topology class characterized by a vorticity value of  $m = 1$ , and their helicities are varied by taking  $\gamma = 0$  and  $\pi$  values for the Néel skyrmions and  $\gamma = -\pi/2$  and  $\pi/2$  values for the Bloch skyrmions. The magnitudes of the spin transport vector quantities show close relation to standard charge current SP-STM images. We demonstrated that the SP-STM images can be used to determine the helicity of the skyrmions. Moreover, we considered the modified spin-polarization vectors of the conduction electrons due to the local chirality of the complex spin texture in the tunneling model. We found that this effect modifies the apparent size of the skyrmions. [33]

We reported high-resolution tunneling electron spin transport properties (longitudinal spin current (LSC) and spin transfer torque (STT) maps) of skyrmionic spin structures with various topological charges ( $Q = -3, -2, -1, 0, 1, 2$ ) in the  $(\text{Pt}_{0.95}\text{Ir}_{0.05})/\text{Fe}/\text{Pd}(111)$  ultrathin magnetic film. Using an out-of-plane magnetized SP-STM tip it is found that the maps of the LSC vectors acting on the spins of the magnetic textures and all STT vector components exhibit the same topology as the skyrmionic objects. In contrast, an in-plane magnetized tip generally does not result in spin transport vector maps that are topologically equivalent to the underlying spin structure, except for the LSC vectors acting on the spins of the skyrmionic textures at a specific relation between the spin polarizations of the sample and the tip. The magnitudes of the spin transport vector quantities exhibit close relations to charge current SP-STM images irrespectively of the skyrmionic topologies. Moreover, we find that the STT efficiency (torque/current ratio) acting on the spins of the skyrmions can reach large values up to  $\sim 25$   $\text{meV}/\mu\text{A}$  ( $\sim 0.97$   $h/e$ ) above the rim of the magnetic objects, but it considerably varies between large and small values depending on the lateral position of the SP-STM tip above the topological spin textures. We introduced a simple expression for the STT efficiency to explain its variation. Our calculated spin transport vectors can be used for the investigation of spin-polarized tunneling-current-induced spin dynamics of topologically distinct surface magnetic skyrmionic textures. [55]

## 4. Magnetic nanoparticles

### a. Ground state, dynamics and thermal magnetization switching

We used the deterministic Landau-Lifshitz-Gilbert equation to investigate the nonlinear dynamics of magnetization and the specific loss power in magnetic nanoparticles with uniaxial anisotropy driven by a rotating magnetic field. We proposed a new type of applied field, which is “simultaneously rotating and alternating,” i.e., the direction of the rotating external field changes periodically. We showed that a more efficient heat generation by magnetic nanoparticles is possible with this new type of applied field and we suggested its possible experimental realization in cancer therapy which requires the enhancement of loss energies. [8]

Antiferromagnetic materials hold promising prospects in novel types of spintronics applications. Assessing the stability of antiferromagnetic nanostructures against thermal excitations is a crucial aspect of designing devices with a high information density. In terms of theoretical calculations and numerical simulations we determined the mean switching time of antiferromagnetic nanoparticles in the superparamagnetic limit. We demonstrated that the thermal stability is drastically reduced compared to ferromagnetic particles in the limit of low Gilbert damping, attributed to the exchange enhancement of the attempt frequencies. We also discussed how the system parameters have to be engineered in order to optimize the switching rates in antiferromagnetic nanoparticles. [48]

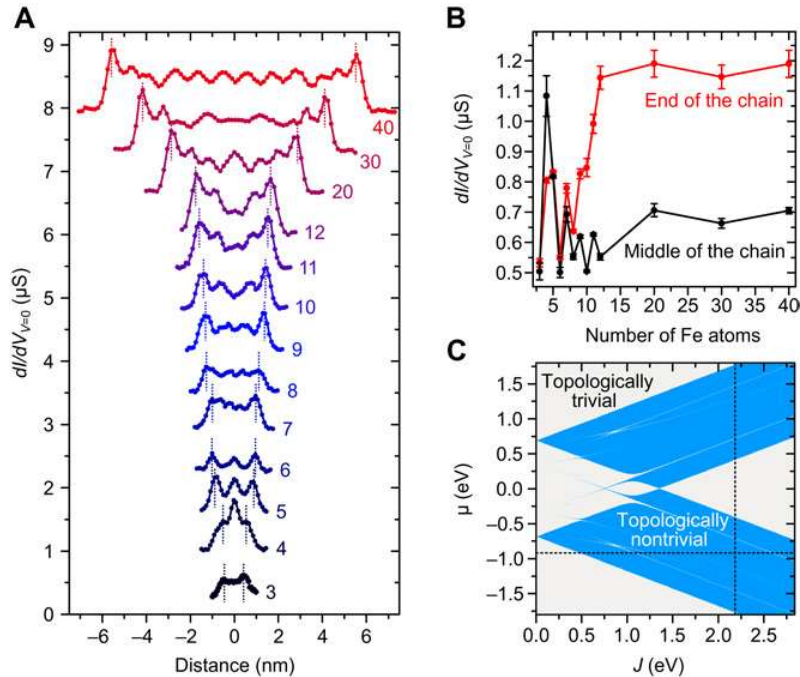
We developed a technique to determine suitable spin models for small embedded clusters of arbitrary geometry by combining the spin-cluster expansion with the relativistic disordered local moment scheme. We presented results for uncovered and covered hexagonal Co clusters on Au(111) surface, and used classical Monte Carlo simulations to study the temperature dependent properties of the systems. For Co clusters covered by Au, both the contribution to the magnetic anisotropy and the easy axis direction of the perimeter atoms differ from those of the inner atoms due to reduced symmetry.

We investigated the spin reversals of the covered clusters with perpendicular magnetic anisotropy and based on the variance of the magnetization component parallel to the easy direction we suggested a technique to determine the blocking temperature of superparamagnetic particles. We also determined the Néel relaxation time from the Monte Carlo simulations and found that it satisfied the Néel-Arrhenius law with an energy barrier close to the magnetic anisotropy energy of the clusters. [20]

Motivated by the challenge of finding Majorana bound states, see later, we performed first-principles calculations of the magnetic properties of Fe chains deposited on the Re(0001) surface. By increasing the length of the chain, a transition is found from an almost collinear antiferromagnetic state for a five-atom-long chain to a spin spiral state with the rotational plane slightly tilted from the surface of the substrate for the 15-atom-long chain. It is shown that a classical spin model derived from the ab initio calculations containing only two-spin interactions supports opposite chirality of the spin spiral compared to a direct optimization of the spin configuration within the ab initio method. The differences between the results of the two methods can be understood by introducing chiral four-spin interactions in the spin model. [42]

### b. Magnetic adatoms on the surface of superconductors

Majorana bound states realized in topological superconductors are expected to play a crucial role in future quantum computing applications. Realizing model-type systems where the signatures of Majorana bound states can be unambiguously identified is a key challenge. Recently single-atomic Fe chains were grown on the Re(0001) surface and the traces of Majorana bound states were investigated by scanning tunneling microscopy experiments. We provided theoretical support by calculating the electronic structure of Fe adatoms adsorbed on the Re(0001) surface. Using the parameters determined from ab initio methods, model calculations indicated that the single-atomic Fe chain may be in the topological superconducting phase. [28]

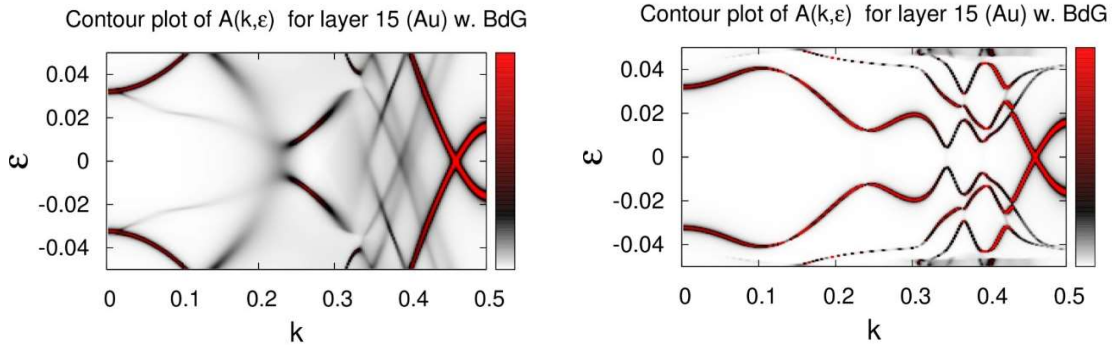


Development and stabilization of enhanced zero-energy LDOS at the ends with increasing chain length and the calculated topological phase diagram for the Fe chain. (A) Measured zero-energy  $dI/dV$  profiles along the chains for (from bottom to the top) 3 to 12, 20, 30, and 40 Fe atoms. (B) Comparison of the variation of zero-energy tunneling conductance between the middle and the ends of the chains with increasing number of atoms. (C) Calculated topological phase diagram for a straight monoatomic Fe chain with noncollinear magnetization as a function of the on-site energy  $m$  and spin splitting parameter  $J$ . Blue and gray shaded regions correspond to the topologically nontrivial superconducting phase and the trivial phase, respectively. The two dotted lines represent the parameters determined from ab initio calculations for Fe on the Re(0001) surface,  $m = -0.92$  eV and  $J = 2.18$  eV. [28]

It was revealed via scanning tunnel spectroscopy and ab initio calculations of a series of 3d transition metal atoms (Mn, Fe, Co) adsorbed on the heavy-element superconductor Re that the increase of the Kondo coupling and sign change in magnetic anisotropy with d-state filling is accompanied by a shift of the Yu-Shiba-Rusinov (YSR) states through the energy gap of the substrate and a crossing of the Fermi level. The uncovered systematic trends enable the identification of the most promising candidates for the realization of topological superconductivity in arrays of similar systems. [49]

## 5. Ab initio study of superconductor – normal metal heterojunctions

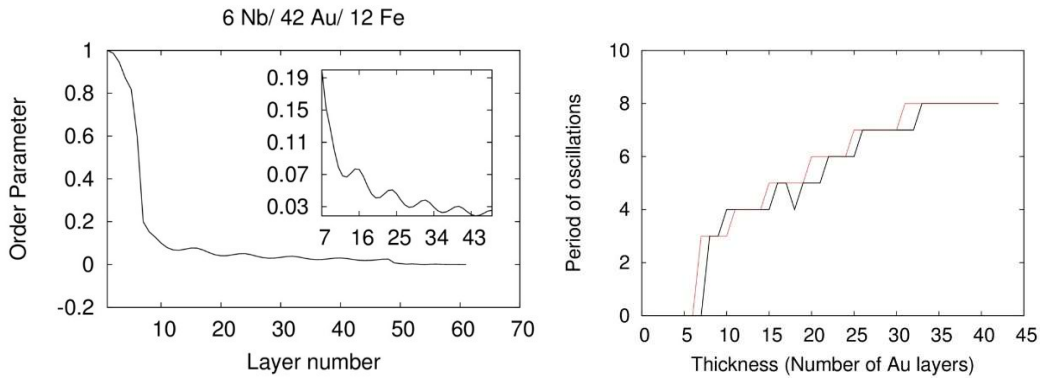
We studied the proximity effect in superconductor–normal metal heterostructures based on first principles calculations with treating the pairing potential as an adjustable parameter. The superconducting order parameter (anomalous density) was obtained from the Green-function by solving the Kohn–Sham–Bogoliubov–de Gennes (KSBdG) equations with the Screened Korrington–Kohn–Rostoker method. The theory were interpreted for Au/Nb(0 0 1) multilayers [5,6,7]. The layer resolved anomalous spectral function was also obtained closely related to the superconducting order parameter. We calculated Shockley-type surface states from the KSBdG equations in the case of the investigated Nb/Au heterostructure along the direction  $k_y=0$ . First, setting the  $\Delta_{\text{Nb}}=0$  Ry, see the left panel of the figure below, the surface state can be observed in the normal state electronic structure. While applying a finite  $\Delta_{\text{Nb}}$  pairing potential does open up a gap in the Au states, similarly to the case of  $k_x=k_y$  direction, but no gap opens at the crossing of the surface state bands, indicating that it does not couple to the superconductor (see right panel of the figure). This effect can be attributed to the fact that obviously the surface state is quite localized to the top layers of the metal surface and it is mainly isolated from the bulk states. Consequently, they do not take part in the Andreev scattering process and thus they do not have a gap in the spectrum, as it can be seen in the below figure. As we indicated earlier, an opposite behavior could be observed for the interface state, which is localized to the Nb/Au interface. The energy of these states shifts upwards. This can be explained by the stronger interaction between the superconductor and the normal metal resulted in a larger gap than in the QW states. [6]



Contour plot of the BSF in the  $k_y=0$  direction corresponding the last layer of Au. The Au sample consisted 9 layers. The quasiparticle spectrum was calculated from the BdG equations.  $\Delta_{\text{Nb}}=0$  Ry is used on the left panel and  $\Delta_{\text{Nb}}=0.05$  Ry on the right panel. [6]

To investigate what happens when the Nb/Au is in the superconducting state and a thin ferromagnetic iron layer is placed in contact with it, we used a semi-phenomenological parametrization of the electron-phonon coupling. Namely, we choose the electron-phonon coupling in the Nb to reproduce the experimental value of the gap (0.2 mRy) in the bulk Nb. We used this value for all Nb layers, and zero electron-phonon coupling was assumed for the Fe layers. For this situation the quasiparticle DOS was calculated from the solution of the fully relativistic, spin polarized Dirac-Bogoliubov-de Gennes (DBdG) equations. [29] We placed different number of Au layers (up to 42) between the Nb and Fe layers, where a perfect face-centered cubic growth is assumed for the Au overlayers. While the results show that the Au layers remained non-magnetic, spin-polarized bands around the Fermi level can be observed. This is the consequence of the different confinement for the spin-up and spin-down

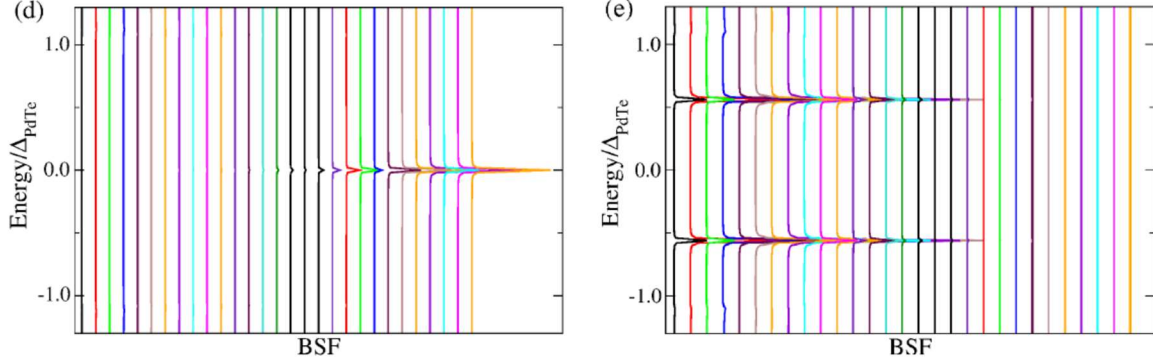
electrons. In fact, quantum-well states are splittings of the band of single-electron states into a series of subbands (caused by the quantization of the electron motion) which depends on the thickness of confinement. As our studies suggested, the spin up electrons are confined in the Au layers only, while the spin down electrons experience a confinement in both the Au and Fe layers. Therefore, due to the different confinement lengths between the spin channels, more bands are observed for the spin-up states than for the spin-down states. Calculations were performed for various directions of the exchange field, however, we found that they all lead to a very similar behavior, only the very fine details of the band structure changes around the Fermi energy. Since, the order parameter is influenced mostly by the states in the close vicinity of the Fermi level, we can conclude that a pairing state (in the Au) can occur between two electrons on the induced split parts of the Fermi surface caused by the quantum well states. Hence, the Cooper pair can acquire a finite momentum leading to the oscillation of the order parameter, analogously to the Fulde-Ferrell-Larkin-Ovchinnikov (FFLO) state. While SOC in Au is rather strong, it does not have significant effect on this process, since the spin-degeneracy was already lifted by the reflection at the normal metal / ferromagnet interface. Compared to the SOC=0 case the main difference is the splitting of the interface states at the Nb/Au interface, however, the impact of this effect on the order parameter appears to be negligible. By solving the DBdG equations self-consistently (assuming again the experimental bulk electron-phonon coupling in the Nb layers, and zero elsewhere) we found an oscillating behavior of the order parameter shown in the below figure. The period of these oscillations depends on the number of Au overlayers since the band structure and the number of quantum well states depends on the thickness of the Au. The order parameter was calculated as a function of the number of Au overlayers up to 42 layers in two cases: with 12 and 24 Fe layers, and the period of the oscillations has been obtained and plotted in both cases in the figure. [29]



**Left:** Order parameter for the Nb/Au/Fe(001) system with 42 gold and 12 Fe overlayers. The inset shows the order parameter in the gold layers. The order shows an oscillating behavior with a period of 8 layers. **Right:** The oscillations' period of the order parameter as a function of the number of gold overlayers in case of 12 Fe (black line) and 24 Fe (red line) layers. [29]

For thicker Au overlayers as the number of the quantum well states are increasing, the bands in the spin up and spin down channel are separated by smaller and smaller  $\mathbf{q}$  vectors. Therefore, the Cooper pairs may acquire smaller and smaller finite momentum, which leads to an increase of the period of oscillation as a function of the Au thickness as observed in the above figure. Our theoretical finding explains the oscillating behavior of the order parameter found in the experiments of H. Yamazaki and coworkers (RIKEN Accel. Prog. Rep. **48**, 253 (2015)). The order parameter in the Au enters the boundary conditions for superconductivity, hence it influences the  $T_c$  as well. Yamazaki *et al.* also found oscillations in the critical temperature with a period of 9 layers. Our results suggest that these  $T_c$  oscillations observed in that experiment may also be a consequence of the interplay between the quantum-well states and ferromagnetism. We mention that the inclusion of more and more Au layers leads to more and more damped oscillations in the Fe layers similarly as it was found in the literature. [29]

In a recently submitted work (Kyungwha Park, Gabor Csire, Balazs Ujfalussy, arXiv:2005.02570) we obtained a very similar scenario for the topological superconductor PdTe/Bi<sub>2</sub>Se<sub>3</sub> overlayer system as in the Nb/Au system. Here we chose PdTe as a superconductor matching epitaxially the Bi<sub>2</sub>Se<sub>3</sub> topological insulator overlayers. The main feature of such materials is the topological surface state, which we studied with the Fermi energy chosen to be right at the surface state as well. In addition to the surface state, there is also an interface state present. It was found that if the Fermi energy is at the Dirac point, and there is no effective pairing interaction in the Bi<sub>2</sub>Se<sub>3</sub> overlayer, then there is no gap induced in the surface state for 4 quintuple layers, while the interface state is split. Based on our detailed studies, we found that the Dirac surface state does not participate in the Andreev scattering process.



Layer-resolved SC-state BSF vs energy in 5-QL/PdTe at  $k_x = 0.01369 \pi/a$  (left) and  $0.03700 \pi/a$  (right) with  $\mu_2 = -0.2884$  Ryd. The BSF of each layer is shifted and scaled. [arXiv:2005.02570]

However, using the electron phonon interaction parameter obtained in the literature, a self-consistent effective pair interaction can be calculated, and then a gap can be obtained. These results are summarized in the following table.

	$\Delta_{\text{EFF}}^{\text{TI}} \neq 0$	$\Delta_{\text{EFF}}^{\text{TI}} = 0$
QWS3	0.220	0.200
QWS2	0.110	0.080
QWS1	0.056	0.016
SS	0.030	0.000

Induced spectral gaps (in units of the bulk SC gap,  $\Delta_{\text{PdTe}} = 0.001$  Ry) for the 5-QL overlayer on SC PdTe at chemical potential  $\mu_4 = -0.2540$  Ry with two different TI pairing potentials  $\Delta_{\text{EFF}}^{\text{TI}}$ . A smaller gap is chosen when two gaps are found at  $k_x$  values close to each other. QWS1, QWS2, QWS3, and SS denote the first lowest, second, and third QWS in the TI conduction band region and the topsurface TI Dirac state, respectively. Due to the numerical accuracy, any gap size  $< 10^{-6}$  Ry is set to zero. [arXiv:2005.02570]

The table also shows the size of the induced gaps in the various Quantum Well states if the Fermi energy is chosen to fall in the energy region away from the Dirac point. Experimental techniques try to tune the Fermi energy by doping the superconductor.

## 6. Topological phases in solids

Somewhat out of the mainstream of our research project, we also explored materials and physical properties where spin-orbit coupling leads to novel topological phases.

The band bending (BB) effect on the surface of the second-generation topological insulators implies a serious challenge to design transport devices. Our self-consistent calculations in the Korringa–Kohn–Rostoker framework showed that in contrast to the bulk bands, the spectrum of the surface states (SSs) is not bent at the surface. In turn, it is possible to tune the energy level of the Dirac point via the deposited surface dopants. In addition, the electrostatic modifications induced by the charged impurities on the surface induce long range oscillations in the charge density. For dopants located beneath the surface, however, these oscillations become highly suppressed. Our findings are in good agreement with recent experiments, however, our results indicate that the concentration of the surface doping cannot be estimated from the energy shift of the Dirac cone within the scope of the effective continuous model for the protected SSs. [3]

We presented a generic effective model describing graphene based hybrid systems where a single sheet of carbon atoms is integrated in to a mesh of BiTeX ( $X=I,Cl,Br$ ) type heterostructures. The rich phase diagram of the model was explored in detail revealing trivial and time reversal invariant topological insulating phases. Experimentally relevant conductivity measurements were also performed in order to identify smoking gun signatures of the emerging topological insulator [42]. In tight collaboration with experimentalists, we reported the first isolation of a single layer of BiTeI monolayer. The performed ab-initio calculations and experimental findings unequivocally confirmed the presence of this new two-dimensional material [24]. We derived a low energy Dirac Hamiltonian for BiTeX/graphene hybrid systems and obtained an analytical phase diagram in terms of spin-orbit coupling, Kekulé distortion strength, uniaxial strain. [59] We explored the electronic structure and topological phase diagram of heterostructures formed of graphene and ternary bismuth-telluro halide layers. We showed that mechanical strain inherently present in fabricated samples could induce a topological phase transition in single-sided heterostructures, turning the sample into a novel experimental realization of a time reversal invariant topological insulator. We constructed an effective tight binding description for low energy excitations and fitted the model's parameters to ab initio band structures. We proposed a simple approach for predicting phase boundaries as a function of mechanical distortions and hence gained a deeper understanding on how the topological phase in the considered system may be engineered. [53, 52]

Signatures of gapless topological phases were examined in magneto-oscillation spectra of nodal loop semimetals. It was found that depending on the direction of the magnetic field two regimes can be separated. In one regime only oscillations with trivial Berry phases are present, while in the other regime a mixture of trivial and topological oscillations can coexist. This study explained hitherto ununderstood experimental findings in these novel materials. [36]

Topological properties of quantum systems could provide protection of information against environmental noise, and thereby drastically advance their potential in quantum information processing. We proposed and studied a topologically protected quantum gate, based on a one-dimensional single-particle tight-binding model, known as the Su-Schrieffer-Heeger chain. The proposed Y gate acts in the two-dimensional zero-energy subspace of a Y junction assembled from three chains and is based on the spatial exchange of the defects supporting the zero-energy modes. In terms of numerical simulations, we demonstrated that the gate is robust against hopping disorder but is corrupted by disorder in the on-site energy. Then we showed that this robustness is due to topological protection, which arises as a joint consequence of chiral symmetry, time-reversal symmetry, and the spatial separation of the zero-energy modes bound to the defects. [50]

$Mn_3Sn$  has recently attracted considerable attention as a magnetic Weyl semimetal exhibiting concomitant transport anomalies at room temperature. The topology of the electronic bands, their relation to the magnetic ground state and their nonzero Berry curvature lie at the heart of the problem. The examination of the full magnetic Hamiltonian reveals otherwise hidden aspects of these unusual physical properties. Our experimental coworkers from Seoul National University (Korea) measured

the full spin wave spectra of Mn<sub>3</sub>Sn over a wide momentum—energy range by the inelastic neutron scattering technique. Using a linear spin wave theory, we determined a suitable magnetic Hamiltonian which not only explains the experimental results but also stabilizes the low-temperature helical phase, consistent with our DFT calculations. The effect of this helical ordering on topological band structures was further examined using a tight binding method, which confirmed the elimination of Weyl points in the helical phase. Our work provided a rare example of the intimate coupling between the electronic and spin degrees of freedom for a magnetic Weyl semimetal system. [39]

## Summary

In the past five years our consortium performed extensive theoretical research in the field of spintronics, nanomagnetism and superconductivity. Based on advanced multi-scale simulations including first-principles electronic calculations and spin-model simulations we studied several phenomena of fundamental and technological interest, such as the exchange bias phenomenon in layered heterostructures, noncollinear magnetic ground states and finite temperature magnetism in bulk and thin film systems, as well as magnetic nanoparticles, to name a few. Our most important results are related to the static, dynamic and thermal properties of magnetic skyrmions in ultrathin films (Sections 3 b and c) and to magnetic adatoms at superconducting surfaces (Section 4b). The study of hybrid normal metal – superconductor heterostructures (Sec. 5) also lies at the heart of our recent and future research in the emerging field of topological superconductivity. We profited a lot from the collaboration with the group of Prof. Roland Wiesendanger at the University of Hamburg. In almost all research topics we had strong collaboration with the group of Prof. Ulrich Nowak at the University of Konstanz. Further collaborations at the University of Bristol and University of York in UK were also essential in our work. In a nutshell, we published 57 scientific research papers with a cumulative impact factor of 221. Despite of the relatively short time frame involved these works attracted at least 330 external citations already. It should also be mentioned that during the period of this OTKA project four of our post-graduate students (András Deák, Levente Rózsa, Gábor Csire and László Balogh) received PhD degree, Levente Rózsa obtained a Humboldt Research Fellowship at the University of Hamburg, Eszter Simon and András Deák won postdoctoral OTKA projects, while Krisztián Palotás won a young-researcher OTKA project. Moreover, the principal investigators won the OTKA project no. K131938 providing basic support for our future scientific activity.